SUPPLEMENTARY INFORMATION

Quantitative Atomic Force Microscopy Provides New Insight into Matrix Vesicle Mineralization

Justin S. Plaut,[a,b] Agnieszka Strzelecka-Kiliszek,[c] Lukasz Bozycki,[c] Slawomir Pikula,[c] René Buchet,[d] Saida Mebarek,[d] Meriem Chadli,[d] Maytê Bolean,[e] Ana M. S. Simao,[e] Pietro Ciancaglini,[e] Andrea Magrini,[f,g] Nicola Rosato,[g,h] David Magne,[e] Agnès Girard-Egrot,[e] Colin Farquharson,[i] Sadik C. Esener,[a,b] José L. Millan,[j] Massimo Bottini*[,g,h,j]

[a] Cancer Early Detection Advanced Research Center, Knight Cancer Institute, Oregon Health & Science University, Portland, Oregon 97201, USA

[b] Department of Bioengineering, University of California San Diego, La Jolla, California 92093, USA

[c] Laboratory of Biochemistry of Lipids, Nencki Institute of Experimental Biology, Polish Academy of Sciences, 02-093 Warsaw, Poland

[d] Université de Lyon, Université Lyon 1, Institut de Chimie et Biochimie Moléculaires et Supramoléculaires, UMR CNRS 5246, 69 622 Villeurbanne Cedex, France

[e] Faculdade de Filosofia, Ciências e Letras de Ribeirão Preto – USP, Departamento de Química, 14040-901 Ribeirão Preto, Brasil

[f] Department of Biopathology and Imaging Diagnostics, University of Rome Tor Vergata, Rome, Italy

[g] Nanoscience & Nanotechnology & Innovative Instrumentation (NAST) Centre, University of Rome Tor Vergata, Rome, Italy

[h] Department of Experimental Medicine, University of Rome Tor Vergata, Rome, Italy

[i] Division of Developmental Biology, The Roslin Institute and Royal (Dick) School of Veterinary Studies, University of Edinburgh, Easter Bush, Roslin, Midlothian, Edinburgh EH25 9RG, UK

[j] Sanford Burnham Prebys Medical Discovery Institute, La Jolla, CA 92037, USA

Supplementary Figures

Supplementary Methods

Probe characterization by scanning electron microscopy. After peak force quantitative nanomechanical mapping, the used Peakforce-HiRs-F-A atomic force microscope probes were cleaned by dipping 5x in water, acetone, methanol, and isopropanol and documented using a Helios Nanolab 660 DualBeam microscope (FEI Materials & Structural Analysis Division, Hillsboro, OR). Micrographs were acquired in immersion mode with a through the lens detector (TLD) at 10 kV accelerating voltage, 25 pA beam current, and 4.6 mm working distance. Images of the tip were acquired from the front and side of the cantilever with 45º stage tilt. Probe vertical half angle and end radius of curvature were measured in ImageJ [1] by averaging measurements taken from the front and side and measured from the terminal 100 nm of the tip.

Indentation model fitting of matrix vesicle force curves. Force curves corresponding to regions of high, moderate, and low indentation depth (relative to the entire data set) of matrix vesicles were extracted from the peak force capture data files in Nanoscope Analysis 1.9. Each force curve was baseline corrected over the initial 10–50% of the loading (approach) curve tip-sample separation and indentation analyses were performed using the Briscoe-Sebastian-Adams (conical-spherical) [2], the Hertzian (spherical) [3], and the Sneddon (conical) [4] indenter models.

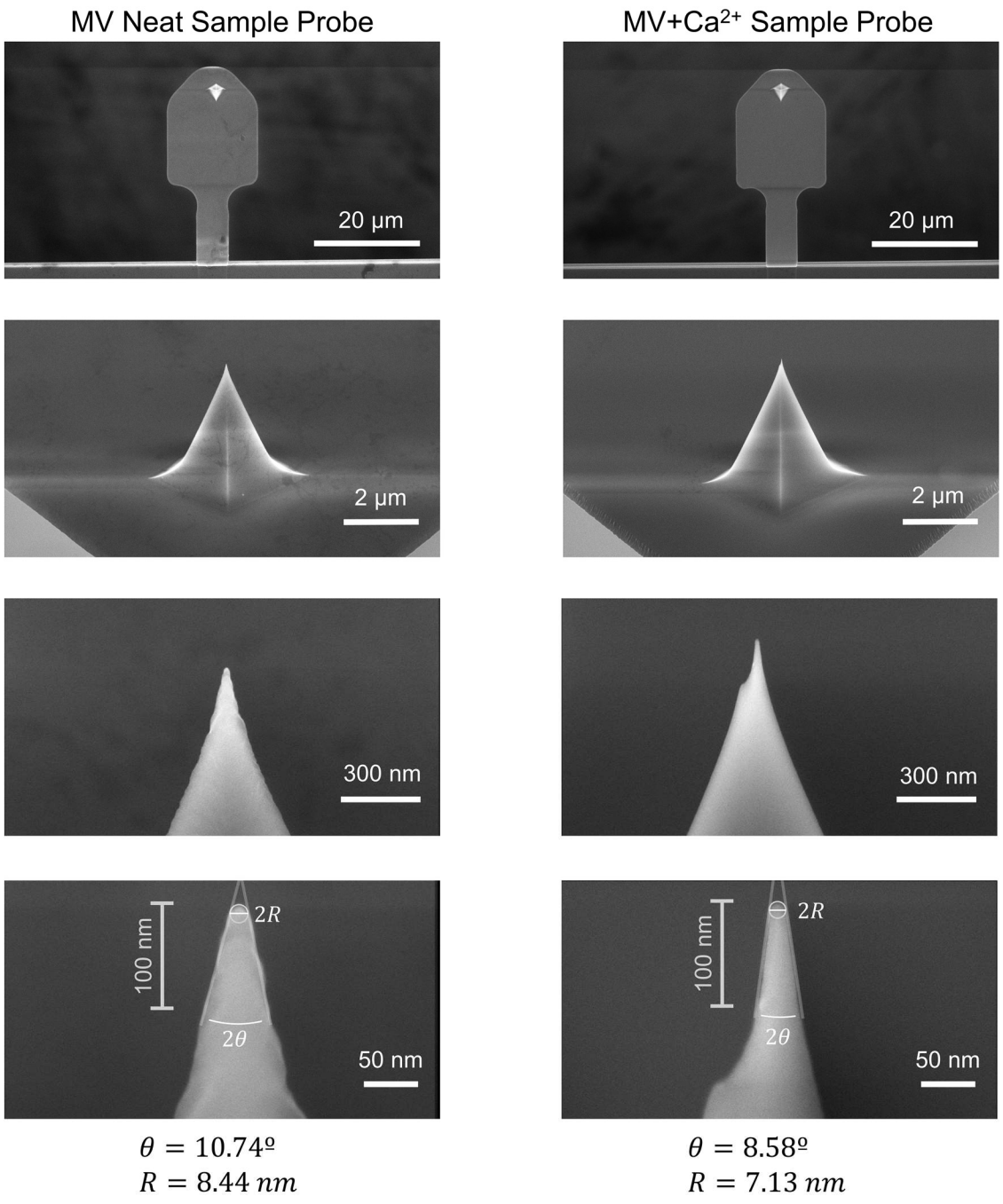

Figure S1. Geometric characterization of atomic force microscope probes by scanning electron microscopy. Electron micrographs show that the terminal 300 nm of the MV Neat probe shank and the terminal 150 nm of the MV+Ca^{2+} probe shank can be closely approximated as conical. From the highest magnification micrograph (and from a side view, not shown), the probe end radius of curvature, R, and the vertical half-angle, θ, were measured. These values were used for all indentation analyses. In vertical order, magnifications are: 5000x, 35000x, 250000x, 1Mx.

For all models, applied force is calculated by Hooke's Law

$$F = k\,z = k\,S_{DS}\,V_{PD}$$

Parameter a is determined implicitly and parameter b is determined explicitly by

$$\delta + \frac{a}{R}\left(\sqrt{a^2 - b^2} - a\right) - \frac{a}{\tan\theta}\left[\frac{\pi}{2} - \sin^{-1}\left(\frac{b}{a}\right)\right] = 0, \qquad b = R\cos\theta$$

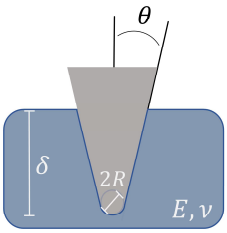

For $\boldsymbol{\delta \gg R}$ the Sneddon **conical** model applies

$$F = \frac{2\,E}{\pi\,(1-\nu^2)}\,\delta^2 \tan\theta$$

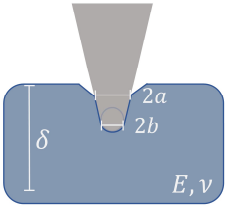

For $\boldsymbol{a > b}$ and $\boldsymbol{\delta \gg R}$ the Briscoe-Sebastian-Adams (BSA) **conical-spherical** model applies

$$F = \frac{2\,E}{1-\nu^2}\left[a\,\delta - \frac{a^2}{2\,\tan\theta}\left[\frac{\pi}{2} - \sin^{-1}\left(\frac{b}{a}\right)\right] - \frac{a^3}{3\,R} + \sqrt{a^2 - b^2}\left(\frac{b}{2\tan\theta} + \frac{a^2 - b^2}{3\,R}\right)\right]$$

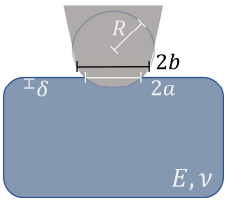

For $\boldsymbol{a \leq b}$ the Hertzian **spherical** model applies (BSA uses this for $a \leq b$)

$$F = \frac{4\,E}{3\,(1-\nu^2)}\,\delta^{3/2}\,R^{1/2}$$

Where,
F: force applied by probe (pN)
k: cantilever spring constant (pN/nm)
S_{DS}: cantilever deflection sensitivity (nm/V)
V_{PD}: photodetector output from cantilever deflection (V)
z: cantilever deflection (nm)
a: maximal cone contact radius (nm)
E: elastic modulus (MPa)
ν: Poisson's ratio (0.5)
δ: sample indentation (nm)
θ: probe vertical half angle (°)
R: probe end radius of curvature (nm)
b: end radius of conical geometry (nm)

Figure S2. Indentation models for elastic modulus determination as applicable to a conical indenter with a semispherical end geometry. In theory, the model is selected by comparing the indentation depth to the radius of curvature of the end geometry. For large indentations, the contact area of the conical portion of the indenter is significantly greater than the contact area of the semispherical end such that the semispherical portion does not significantly affect the overall indentation behavior and can be ignored (Sneddon conical model) [4]. For moderate indentations, both the conical region and semispherical end significantly contribute to the indentation behavior (Briscoe-Sebastian-Adams conico-spherical model) [2]. For small indentations, only the semispherical portion is involved in the indentation process (Hertzian spherical model) [3].

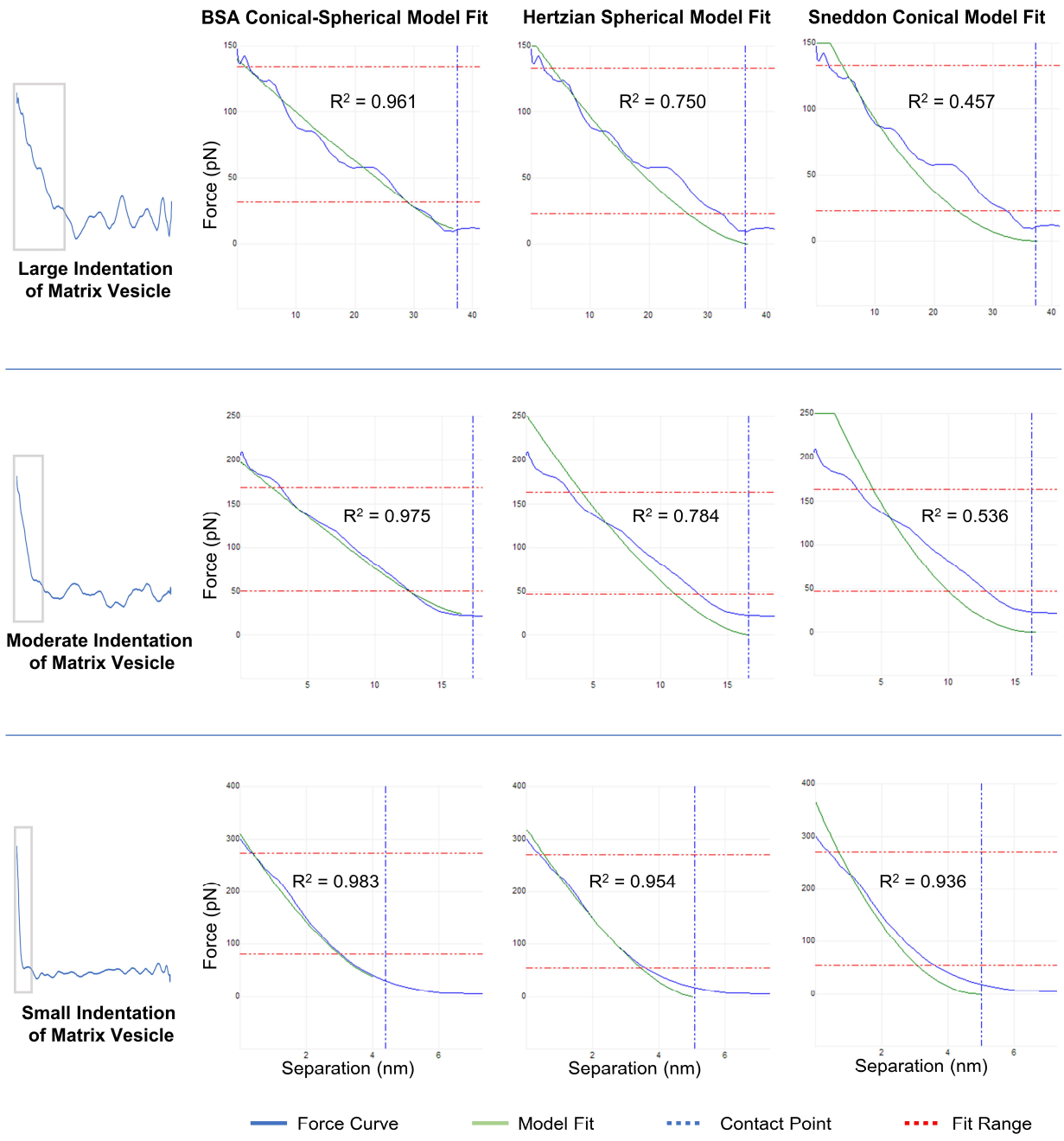

Figure S3. Indentation model fitting of force curves acquired from matrix vesicles shows that the BSA conical-spherical indenter model best fits the data. Representative force curve corresponding to large, moderate, and small indentations of MVs are shown with curve fitting from each of the three models. The quality of fit was determined qualitatively by how well the model tracks the trajectory of the force curve over the entire sample contact region and by the coefficient of determination, R^2, calculated over the fit region (15–80% of maximum force). The low indentation fits for the Hertzian and Sneddon models show high R^2 values, but the trajectories diverge at both ends of the contact region. The full force curves and their regions of analysis are shown to the left.

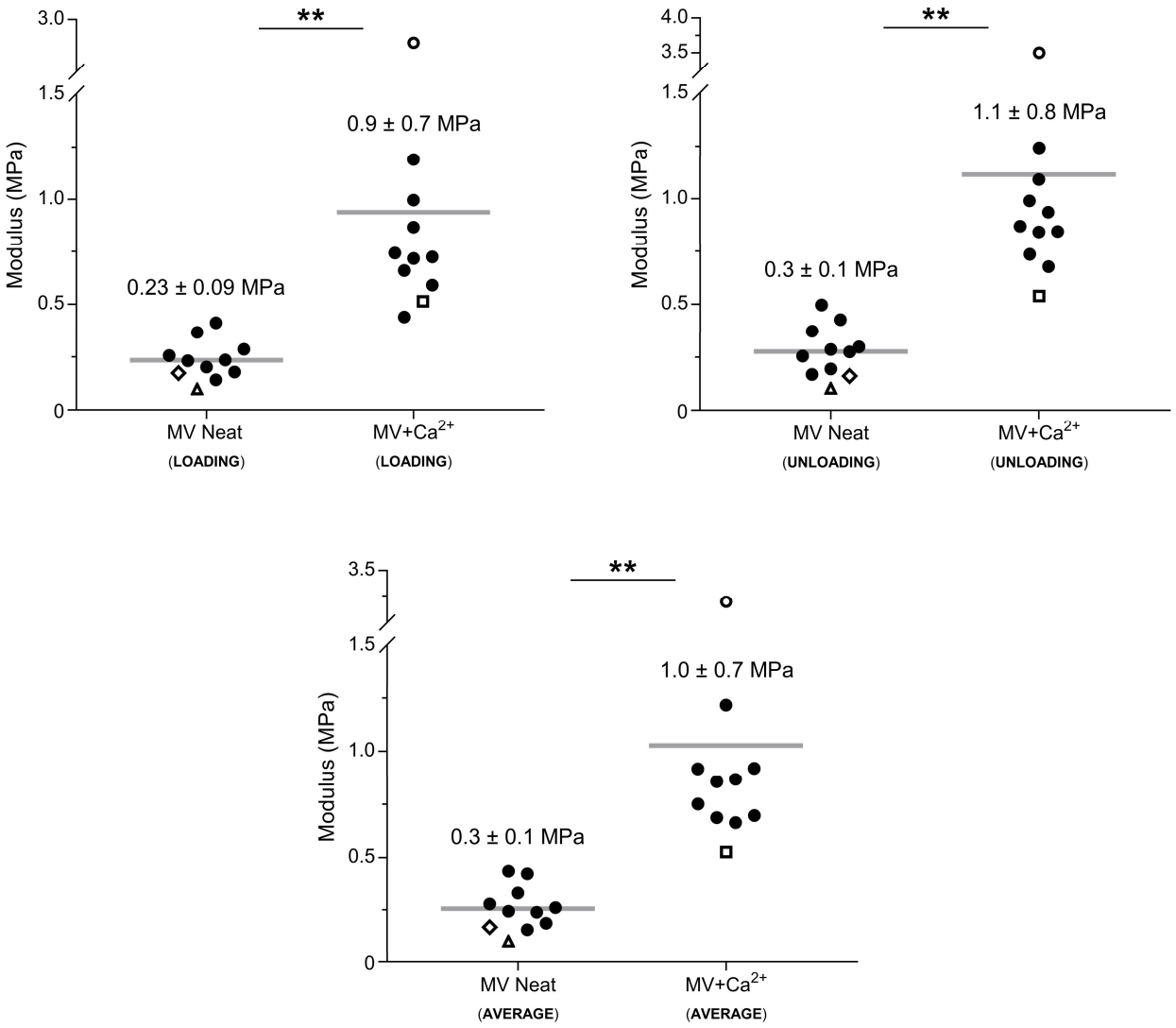

Figure S4. Elastic moduli of matrix vesicles calculated from loading, unloading, and averaged loading and unloading curves. Elastic modulus data was calculated from AFM micrographs of individual vesicles acquired in PFQNM mode (n = 11 vesicles per group). Each marker corresponds to the average elastic modulus of a single MV and the horizontal bar is the mean of the group (mean ± standard deviation shown). Hollow markers correspond to individual MVs shown in Figures 2 and 3 of the main text. Due to minimal hysteresis between the loading and unloading curves and the presence of strong adhesion in the unloading curves of >85% of the MVs measured, the loading curves provided a more accurate fit. The following articles are published examples of these three methods of calculation as applied to biological samples: loading curves [5-9], unloading curves [10, 11], and averaged loading and unloading curves [12-15].

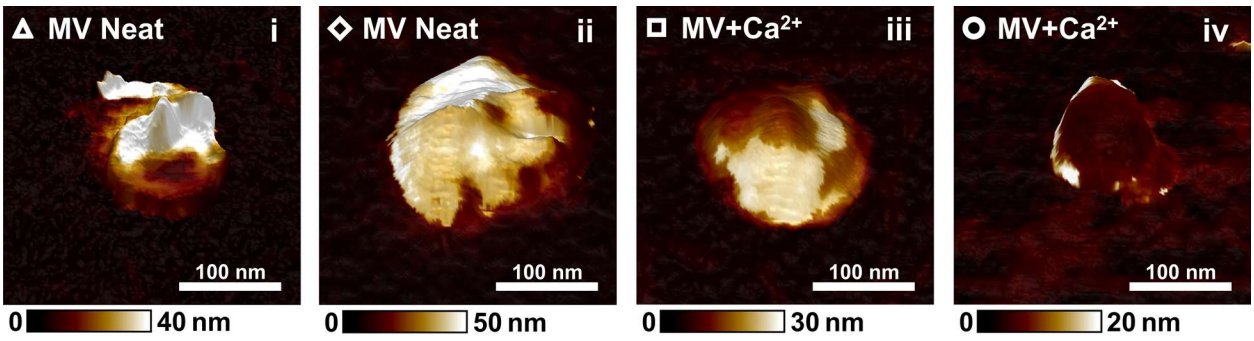

Figure S5. Three-dimensional renderings of individual matrix vesicles with overlaid colorimetric deformation map as measured by AFM-PFQNM. Greater deformation is observed for vesicles from the MV Neat sample (i–ii) compared to the MV+Ca^{2+} sample (iii–iv). The tall, deformable topographic peak observed in (i) is characteristic of vesicles in the MV Neat sample. This peak is obfuscated in (ii) as this highly deformable vesicle was not compressed to the same extent as (i) and thus its internal contents were not revealed during imaging. The relatively less deformable peak observed in (iii) and the absence of a peak in (iv) is characteristic of vesicles in the MV+Ca^{2+} sample. The hollow symbols correspond to the elastic modulus data points shown in Figure 2C of the main text.

Supplementary References

[1] C.A. Schneider, W.S. Rasband, K.W. Eliceiri, NIH Image to ImageJ: 25 years of image analysis, Nat. Methods 9(7) (2012) 671-5.

[2] B.J. Briscoe, K.S. Sebastian, M.J. Adams, The Effect of Indenter Geometry on the Elastic Response to Indentation, J. Phys. D Appl. Phys. 27(6) (1994) 1156-1162. https://doi.org/10.1088/0022-3727/27/6/013.

[3] H. Hertz, Über die Berührung fester elastischer Körper, J. Reine Angew. Math 92(1882) (1882) 156-171. https://doi.org/10.1515/crll.1882.92.156.

[4] I.N. Sneddon, The relation between load and penetration in the axisymmetric boussinesq problem for a punch of arbitrary profile, Int. J. Eng. Sci. 3(1) (1965) 47-57. https://doi.org/10.1016/0020-7225(65)90019-4.

[5] C. Rotsch, F. Braet, E. Wisse, M. Radmacher, AFM imaging and elasticity measurements on living rat liver macrophages, Cell Biol. Int. 21(11) (1997) 685-96. https://doi.org/10.1006/cbir.1997.0213.

[6] L.R. Nyland, D.W. Maughan, Morphology and Transverse Stiffness of Drosophila Myofibrils Measured by Atomic Force Microscopy, Biophys. J. 78(3) (2000) 1490-1497. https://doi.org/10.1016/s0006-3495(00)76702-6.

[7] F. Rico, P. Roca-Cusachs, N. Gavara, R. Farre, M. Rotger, D. Navajas, Probing mechanical properties of living cells by atomic force microscopy with blunted pyramidal cantilever tips, Phys. Rev. E 72(2 Pt 1) (2005) 021914. https://doi.org/10.1103/PhysRevE.72.021914.

[8] M.J. Rosenbluth, W.A. Lam, D.A. Fletcher, Force microscopy of nonadherent cells: a comparison of leukemia cell deformability, Biophys. J. 90(8) (2006) 2994-3003. https://doi.org/10.1529/biophysj.105.067496.

[9] D.C. Lin, E.K. Dimitriadis, F. Horkay, Robust strategies for automated AFM force curve analysis--I. Non-adhesive indentation of soft, inhomogeneous materials, J. Biomech. Eng. 129(3) (2007) 430-40. https://doi.org/10.1115/1.2720924.

[10] A. Touhami, B. Nysten, Y.F. Dufrêne, Nanoscale Mapping of the Elasticity of Microbial Cells by Atomic Force Microscopy, Langmuir 19(11) (2003) 4539-4543. https://doi.org/10.1021/la034136x.

[11] W. Gindl, T. Schöberl, The significance of the elastic modulus of wood cell walls obtained from nanoindentation measurements, Composites Part A: Applied Science and Manufacturing 35(11) (2004) 1345-1349. https://doi.org/10.1016/j.compositesa.2004.04.002.

[12] J. Domke, M. Radmacher, Measuring the Elastic Properties of Thin Polymer Films with the Atomic Force Microscope, Langmuir 14(12) (1998) 3320-3325. https://doi.org/10.1021/la9713006.

[13] A.J. Engler, L. Richert, J.Y. Wong, C. Picart, D.E. Discher, Surface probe measurements of the elasticity of sectioned tissue, thin gels and polyelectrolyte multilayer films: Correlations between substrate stiffness and cell adhesion, Surf. Sci. 570(1-2) (2004) 142-154. https://doi.org/10.1016/j.susc.2004.06.179.

[14] A.J. Engler, S. Sen, H.L. Sweeney, D.E. Discher, Matrix elasticity directs stem cell lineage specification, Cell 126(4) (2006) 677-89. https://doi.org/10.1016/j.cell.2006.06.044.

[15] D. Docheva, D. Padula, C. Popov, W. Mutschler, H. Clausen-Schaumann, M. Schieker, Researching into the cellular shape, volume and elasticity of mesenchymal stem cells, osteoblasts and osteosarcoma cells by atomic force microscopy, J. Cell. Mol. Med. 12(2) (2008) 537-52. https://doi.org/10.1111/j.1582-4934.2007.00138.x.